Universiteit Gent
Faculteit Wetenschappen
Vakgroep Fysica en Sterrenkunde

No title yet

No sub-title neither, obviously...

Alexis Fagot

Thesis to obtain the degree of
Doctor of Philosophy in Physics
Academic years 2012-2017

Universiteit Gent
Faculteit Wetenschappen
Vakgroep Fysica en Sterrenkunde

Promotoren: Dr. Michael Tytgat
Prof. Dr. Dirk Ryckbosch

Universiteit Gent
Faculteit Wetenschappen

Vakgroep Fysica en Sterrenkunde
Proeftuinstraat 86, B-9000 Gent, België

Tel.: +32 9 264.65.28
Fax.: +32 9 264.66.97

Thesis to obtain the degree of
Doctor of Philosophy in Physics
Academic years 2012-2017

Acknowledgements

Ici on remerciera tous les gens que j'ai pu croiser durant cette aventure et qui m'ont permis de passer un bon moment

Gent, ici la super date de la mort qui tue de la fin d'écriture
Alexis Fagot

Table of Contents

Acknowledgements **i**

Nederlandse samenvatting **xiii**

English summary **xv**

1 Introduction **1-1**
1.1 A story of High Energy Physics 1-1
1.2 Organisation of this study 1-1

2 Investigating the TeV scale **2-1**
2.1 The Standard Model of Particle Physics 2-1
2.2 The Large Hadron Collider and the Compact Muon Solenoid . . . 2-1
2.3 Muon Phase-II Upgrade 2-1

3 Amplification processes in gaseous detectors **3-1**
3.1 Signal formation 3-1
3.2 Gas transport parameters 3-1

4 Resistive Plate Chambers **4-1**
4.1 Principle 4-1
4.2 Rate capability of Resistive Plate Chambers 4-1
4.3 High time resolution 4-1
4.4 Resistive Plate Chambers at CMS 4-1

5 Investigation on high rate RPCs **5-1**
5.1 Rate limitations and ageing of RPCs 5-1
5.1.1 Low resistivity electrodes 5-1
5.1.2 Low noise front-end electronics 5-1
5.2 Construction of prototypes 5-1
5.3 Results and discussions 5-1

6 Consolidation and Research and Development approval **6-1**
6.1 Testing detectors under extreme conditions 6-1
6.1.1 High-Luminosity LHC 6-1
6.1.2 The Gamma Irradiation Facilities 6-1

6.1.2.1 GIF 6-1
6.1.2.2 GIF++ 6-3
6.2 Preliminary consolidation tests at GIF 6-3
6.2.1 Resistive plate chamber test setup 6-3
6.2.2 Data acquisition 6-4
6.2.3 Geometrical acceptance of the setup layout to cosmic muons 6-5
6.2.3.1 Description of the simulation layout 6-6
6.2.3.2 Simulation procedure 6-8
6.2.3.3 Results 6-11
6.2.4 Photon flux at GIF 6-11
6.2.4.1 Expectations from simulations 6-11
6.2.4.2 Dose measurements 6-14
6.3 Consolidation tests at GIF++ 6-14
6.4 Results and discussions 6-14
6.4.1 Preliminary studies results 6-14
6.4.2 Consolidation studies results 6-14

7 Simulating a RPC **7-1**
7.1 Garfield++ simulation 7-1
7.2 Hybrid simulation 7-1
7.3 Results and discussions 7-1

8 Conclusions and outlooks **8-1**
8.1 Conclusions 8-1
8.2 Outlooks 8-1

A A data acquisition software for VME CAEN TDCs **A-1**
A.1 Introduction A-1

B Details on the online analysis package **B-1**
B.1 Introduction B-1

C Structure of the hybrid simulation software **C-1**
C.1 Introduction C-1

List of Figures

2.1 Absorbed dose in the CMS cavern after an integrated luminosity of $3000\,\mathrm{fb}$. R is the transverse distance from the beamline and Z is the distance along the beamline from the Interaction Point at Z=0. 2-2

2.2 A quadrant of the muon system, showing DT chambers (yellow), RPC (light blue), and CSC (green). The locations of new forward muon detectors for Phase-II are contained within the dashed box and indicated in red for GEM stations (ME0, GE1/1, and GE2/1) and dark blue for improved RPC stations (RE3/1 and RE4/1). . . . 2-3

2.3 RMS of the multiple scattering displacement as a function of muon p_T for the proposed forward muon stations. All of the electromagnetic processes such as bremsstrahlung and magnetic field effect are included in the simulation. 2-3

6.1 Layout of the test beam zone called X5c GIF at CERN. Photons from the radioactive source produce a sustained high rate of random hits over the whole area. The zone is surrounded by $8\,\mathrm{m}$ high and $80\,\mathrm{cm}$ thick concrete walls. Access is possible through three entry points. Two access doors for personnel and one large gate for material. A crane allows installation of heavy equipment in the area. 6-2

6.2 ^{137}Cs decays by β^- emission to the ground state of ^{137}Ba (BR = 5.64%) and via the $662\,\mathrm{keV}$ isomeric level of ^{137}Ba (BR = 94.36%) whose half-life is 2.55 min. 6-2

6.3 Description of the RPC setup. Dimensions are given in mm. Figure 6.3a provides a side view of the setup while Figure 6.3b shows a top view. A tent containing RPCs is placed at $1720\,\mathrm{mm}$ from the source container. The source is situated in the center of the container. RE-4-2-BARC-161 chamber is $160\,\mathrm{mm}$ inside the tent. This way, the distance between the source and the chambers plan is $2060\,\mathrm{mm}$. 6-3

6.4 RE-4-2-BARC-161 chamber is inside the tent as described in Figure 6.3. In the top right, the two scintillators used as trigger can be seen. This trigger system has an inclination of 10° relative to horizontal and is placed above half-partition B2 of the RPC. PMTs' electronics are shielded thanks to lead blocks placed in order to protect them without stopping photons from going through the scintillators and the chamber. 6-4

6.5 Hit distributions over all 3 parttions of RE-4-2-BARC-161 chamber is shown in these histograms. Top, middle and bottom histograms respectively correspond to partitions A, B and C. These plots show that some events still occur in strips 33 to 48 while only strips 49 to 64 were recorded on later data taking, contributing to the inefficiency of detection of cosmic muons. 6-5

6.6 Signals from the RPC strips are shaped by the Front End Electronics (FEEs) described on Figure 6.6a. Output LVDS signals are then read-out by a TDC module connected to a computer or converted into NIM and sent to scalers. Figure 6.6b describes how these converted signals are put in coincidence with the trigger. . . 6-6

6.7 Description of the principle of a CFD. A comparison of threshold triggering (left) and constant franction triggering (right) is shown in Figure 6.7a. Constant franction triggering is obtained thanks to zero-crossing technique as explained in Figure 6.7b. The signal arriving at the input of the CFD is split into three components. A first one is delayed and connected to the inverting input of a first comparator. A second component is connected to the noninverting input of this first comparator. A third component is connected to the noninverting input of another comparator along with a threshold value connected to the inverting input. Finally, the output of both comparators is fed through an AND gate. 6-7

6.8 Results are derived from data taken on half-partition B2 only. At GIF, while the number of triggers doesn't depend on the half-partition used during runs, some related events are lost by happening in other half-partitions because of the setup configuration. On the 18^{th} of June 2014, data has been taken on chamber RE-2-BARC-161 at building 904 (Prevessin Site) with cosmic muons providing us a reference efficiency plateau of $(97.54 \pm 0.15)\%$ represented by a black curve. A similar measurement has been done at GIF on the 21^{st} of July with the same chamber giving a plateau of $(78.52 \pm 0.94)\%$ represented by a red curve. 6-8

6.9 Representation of the layout used for the simulations of the test setup. The RPC is represented as a yellow trapezoid while the two scintillators as blue cuboids looking at the sky. A green plane corresponds to the muon generation plane within the simulation. Figure 6.3a shows a global view of the simulated setup. Figure 6.3b shows a zommed view that allows to see the 2 scintillators as well as the full RPC plane. 6-9
6.10 γ flux $F(D)$ is plot using values from table 6.1. As expected, the plot shows similar attenuation behaviours with increasing distance for each absorption factors. 6-12
6.11 Figure 6.11a shows the linear approximation fit done via formulae 6.7 on data from table 6.2. Figure 6.11b shows a comparison of this model with the simulated flux using a and b given in figure 6.11a in formulae 6.4 and the reference value $D_0 = 50cm$ and the associated flux for each absorption factor F_0^{ABS} from table 6.1 6-14
6.12 Dose measurements has been done in a plane corresponding to the tents front side. This plan is $1900\,\mathrm{mm}$ away from the source. As explained in the first chapter, a lens-shaped lead filter provides a uniform photon flux in the vertical plan orthogonal to the beam direction. If the second line of measured fluxes is not taken into account because of lower values due to experimental equipments in the way between the source and the tent, the uniformity of the flux is well showed by the results. 6-15
6.13 6-16

List of Tables

6.1 Total photon flux ($E\gamma \leq 662\,\mathrm{keV}$) with statistical error predicted considering a ^{137}Cs activity of $740\,\mathrm{GBq}$ at different values of the distance D to the source along the x-axis of irradiation field [4]. . 6-11

6.2 Correction factor c is computed thanks to formulae 6.5 taking as reference $D_0 = 50\,\mathrm{cm}$ and the associated flux F_0^{ABS} for each absorption factor available in table 6.1. 6-13

6.3 The data at D_0 in 1997 is taken from [4]. In a second step, using Equations 6.8 and 6.9, the flux at D can be estimated in 1997. Then, taking into account the attenuation of the source activity, the flux at D can be estimated at the time of the tests in GIF in 2014. Finally, assuming a sensitivity of the RPC to γ $s = 2 \cdot 10^{-3}$, an estimation of the hit rate per unit area is obtained. 6-15

List of Acronyms

Nederlandse samenvatting
–Summary in Dutch–

Le resume en Neerlandais (j'aurais peut-etre de apprendre la langue juste pour ca...).

English summary

Le meme résume mais en Anglais (on commencera par la hein!).

1 Introduction

1.1 A story of High Energy Physics

1.2 Organisation of this study

2 Investigating the TeV scale

2.1 The Standard Model of Particle Physics

2.2 The Large Hadron Collider and the Compact Muon Solenoid

2.3 Muon Phase-II Upgrade

After the more than two years lasting first Long Shutdown (LS1), the Large Hadron Collider (LHC) delivered its very first Run-II proton-proton collisions early 2015. LS1 gave the opportunity to the LHC and to the its experiments to undergo upgrades. The accelerator is now providing collisions at center-of-mass energy of $13\,\mathrm{TeV}$ and bunch crossing rate of $40\,\mathrm{MHz}$, with a peak luminosity exceeding its design value. During the first and upcoming second LHC Long Shutdown, the Compact Muon Solenoid (CMS) detector is also undergoing a number of upgrades to maintain a high system performance [1].

From the LHC Phase-2 or High-Luminosity (HL-LHC) period onwards, i.e. past the third LHC Long Shutdown (LS3), the performance degradation due to integrated radiation as well as the average number of inelastic collisions per bunch crossing, or pileup, will rise substantially and become a major challenge for the LHC experiments, like CMS that are forced to address an upgrade program for Phase-II [2]. Simulations of the expected distribution of absorbed dose in the CMS detector under HL-LHC conditions, show in figure 6.12 that detectors placed close

to the beamline will have to withstand high irradiation, the radiation dose being of the order of a few tens ofGy.

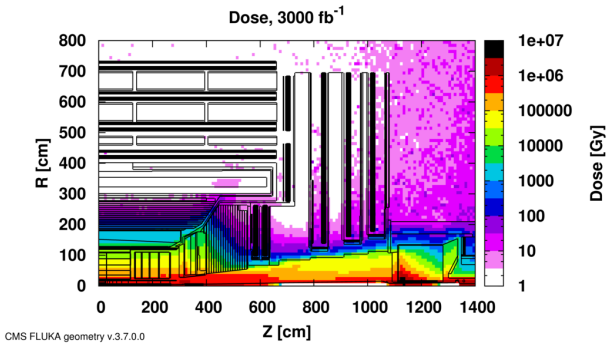

Figure 2.1: Absorbed dose in the CMS cavern after an integrated luminosity of $3000\,\mathrm{fb}$. *R is the transverse distance from the beamline and Z is the distance along the beamline from the Interaction Point at Z=0.*

The measurement of small production cross-section and/or decay branching ratio processes, such as the Higgs boson coupling to charge leptons or the $B_s \longrightarrow \mu^+\mu^-$ decay, is of major interest and specific upgrades in the forward regions of the detector will be required to maximize the physics acceptance on the largest possible solid angle. To ensure proper trigger performance within the present coverage, the muon system will be completed with new chambers. In figure 2.2 one can see that the existing Cathode Strip Chamber (CSC) modules will be completed by Gas Electron Multipliers (GEM) and Resistive Plate Chambers (RPC) in the pseudo-rapidity region $1.6 < |\eta| < 2.4$ to complete its redundancy as originally scheduled in the CMS Technical Proposal [3].

RPCs are used by the CMS first level trigger for their good timing performances. Indeed, a very good bunch crossing identification can be obtained with the present CMS RPC system, given their fast response of the order of $1\,\mathrm{ns}$. In order to contribute to the precision of muon momentum measurements, muon chambers should have a spatial resolution less or comparable to the contribution of multiple scattering [1]. Most of the plausible physics is covered only considering muons with p_T $<100\,\mathrm{GeV}$ thus, in order to match CMS requirements, a spatial resolution of $\mathcal{O}(\text{few } \mathrm{mm})$ the proposed new RPC stations, as shown by the simulation in figure 2.3. According to preliminary designs, RE3/1 and RE4/1 readout pitch will be comprised between 3 and $6\,\mathrm{mm}$ and 5 η-partitions could be considered.

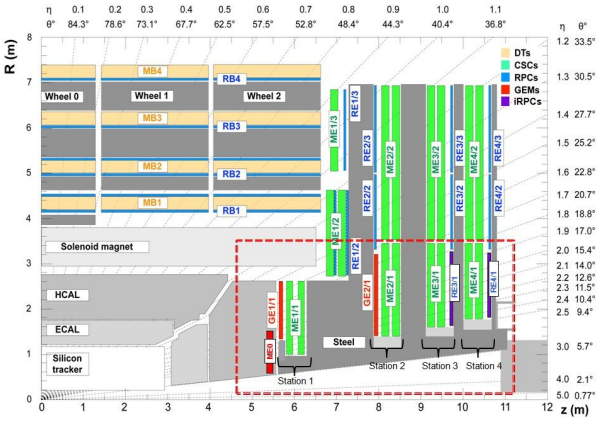

Figure 2.2: A quadrant of the muon system, showing DT chambers (yellow), RPC (light blue), and CSC (green). The locations of new forward muon detectors for Phase-II are contained within the dashed box and indicated in red for GEM stations (ME0, GE1/1, and GE2/1) and dark blue for improved RPC stations (RE3/1 and RE4/1).

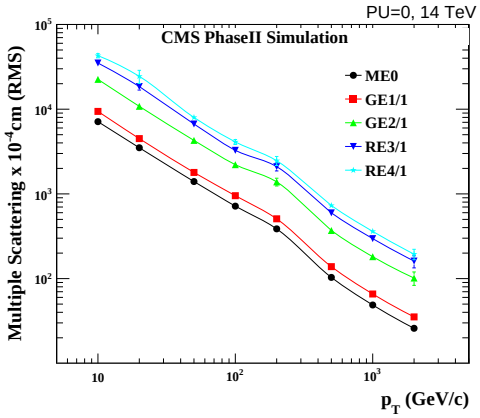

Figure 2.3: RMS of the multiple scattering displacement as a function of muon p_T for the proposed forward muon stations. All of the electromagnetic processes such as bremsstrahlung and magnetic field effect are included in the simulation.

3

Amplification processes in gaseous detectors

3.1 Signal formation

3.2 Gas transport parameters

4

Resistive Plate Chambers

4.1 Principle

4.2 Rate capability of Resistive Plate Chambers

4.3 High time resolution

4.4 Resistive Plate Chambers at CMS

5

Investigation on high rate RPCs

5.1 Rate limitations and ageing of RPCs

5.1.1 Low resistivity electrodes

5.1.2 Low noise front-end electronics

5.2 Construction of prototypes

5.3 Results and discussions

6

Consolidation and Research and Development approval

6.1 Testing detectors under extreme conditions

6.1.1 High-Luminosity LHC

6.1.2 The Gamma Irradiation Facilities

6.1.2.1 GIF

(GIF) was a test area located in the SPS West Area at the downstream end of the X5 test beam in which particle detectors were exposed to a particle beam in presence of an adjustable background flux of photons [**GIFacility**]. This facility's goal was to simulate background conditions these detectors would suffer in their operating environment at the LHC. A schematic layout of the GIF zone is shown in Figure 6.1. Photons are produced by a strong radioactive source of ^{137}Cs installed in the upstream part of the zone inside a lead container, which includes a collimator, designed to irradiate a $6 \times 6\,\mathrm{m}^2$ area at $5\,\mathrm{m}$ distance from the source. A thin lens-shaped lead filter renders the outcoming flux uniform in the vertical plane orthogonal to the beam direction. Control of the photon rate is achieved by further lead filters allowing the maximum rate to be limited and to vary within a range of four orders of magnitude. The Gamma source is located in a rectangular lead container.

As described on Figure 6.2, the ^{137}Cs source with a half-life of 30 years and an

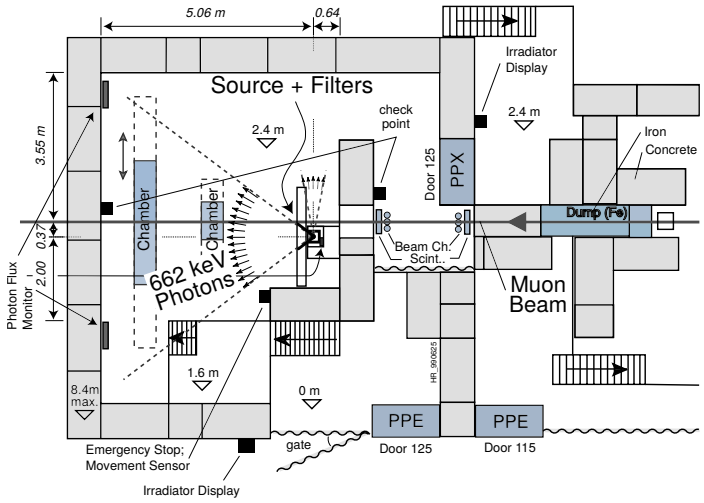

Figure 6.1: Layout of the test beam zone called X5c GIF at CERN. Photons from the radioactive source produce a sustained high rate of random hits over the whole area. The zone is surrounded by $8\,\mathrm{m}$ *high and* $80\,\mathrm{cm}$ *thick concrete walls. Access is possible through three entry points. Two access doors for personnel and one large gate for material. A crane allows installation of heavy equipment in the area.*

activity of $740\,\mathrm{GBq}$, as measured on the 5^{th} March 1997, emits a $662\,\mathrm{keV}$ photon in 85% of the decays. The principal collimator hole provides a pyramidal aperture of $74° \times 74°$ solid angle. This provides a photon flux in a pyramidal volume of $5\,\mathrm{m}$ maximum length along the beam axis.

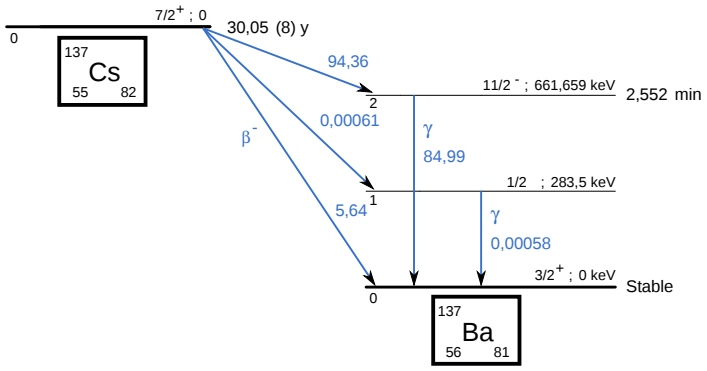

Figure 6.2: ^{137}*Cs decays by* β^- *emission to the ground state of* ^{137}*Ba (BR = 5.64%) and via the* $662\,\mathrm{keV}$ *isomeric level of* ^{137}*Ba (BR = 94.36%) whose half-life is 2.55 min.*

Particle detectors under test are then placed within the pyramidal volume in front of the source, perpendicularly to the beam line in order to profit from the homogeneous photon flux. Adjusting the background flux of photons can then be done by using the filters and choosing the position of the detectors with respect to the source.

6.1.2.2 GIF++

6.2 Preliminary consolidation tests at GIF

6.2.1 Resistive plate chamber test setup

During summer 2014, preliminary tests have been conducted in the GIF area on a newly produced RE4-2 chamber labelled RE-4-2-BARC-161. This chamber has been placed into a trolley covered with a tent. The position of the RPC inside the tent and of the tent related to the source is described in Figure 6.3. To test this CMS RPC, three different absorber settings were used. First of all, measurements were done with fully opened source. Then, to complete this preliminary study, the gamma flux has been attenuated by a factor 2 and a factor 5. The expected gamma flux at the level of our detector will be discussed in subsection 6.2.4.

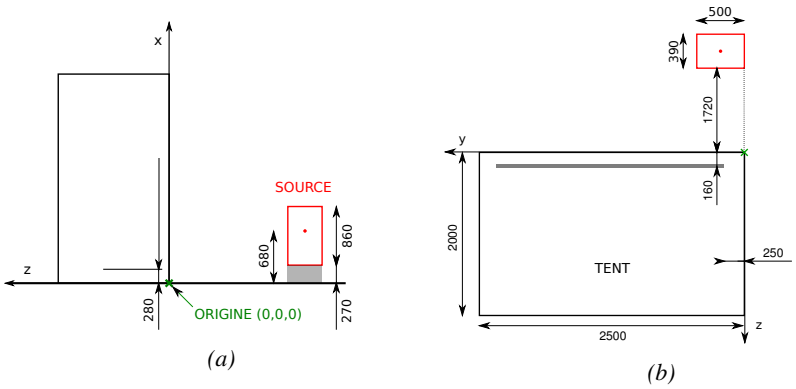

Figure 6.3: Description of the RPC setup. Dimensions are given in mm. *Figure 6.3a provides a side view of the setup while Figure 6.3b shows a top view. A tent containing RPCs is placed at* 1720 mm *from the source container. The source is situated in the center of the container. RE-4-2-BARC-161 chamber is* 160 mm *inside the tent. This way, the distance between the source and the chambers plan is* 2060 mm.

At the time of the tests, the beam not being operationnal anymore, a trigger composed of 2 plastic scintillators has been placed in front of the setup with an inclination of 10 deg ***(this has to be first confirmed by the simulation - I will adjust in consequence cause it has never been precisely measured)*** with respect to

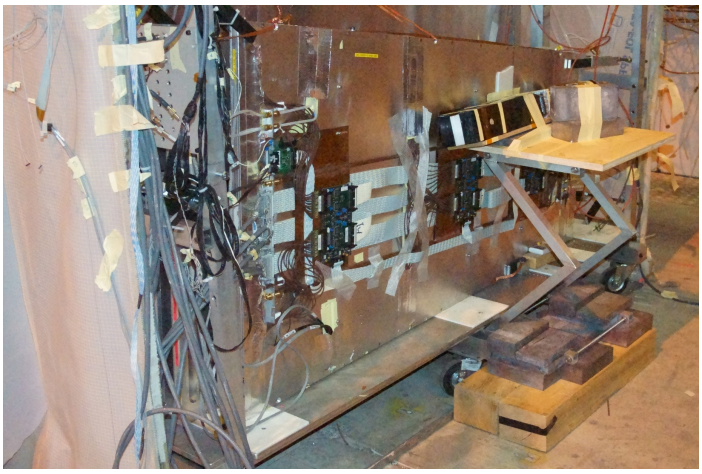

Figure 6.4: RE-4-2-BARC-161 chamber is inside the tent as described in Figure 6.3. In the top right, the two scintillators used as trigger can be seen. This trigger system has an inclination of 10° *relative to horizontal and is placed above half-partition B2 of the RPC. PMTs' electronics are shielded thanks to lead blocks placed in order to protect them without stopping photons from going through the scintillators and the chamber.*

the detector plane in order to look at cosmic muons. Using this particular trigger layout, shown on Figure 6.4, leads to a cosmic muon hit distribution into the chamber similar to the one in Figure 6.5. Measured without gamma irradiation, two peaks can be seen on the profil of partition B, centered on strips 52 and 59. Sub-section 6.2.3 will help us undertand that these two peaks are due respectively to forward and backward coming cosmic particles where forward coming particles are first detected by the scintillators and then the RPC while the backward coming muons are first detected in the RPC.

6.2.2 Data acquisition

Signals induced by cosmic particle in the RPC strips are shaped by standard CMS RPC Front End Electronics (FEE) following the scheme of Figure 6.6. On a first stage, analogic signals are amplified and then sent to the constant fraction discriminator (CFD) described in Figure 6.7. At the end of the chain, $100\,\mathrm{ns}$ long pulses are sent in the LVDS output. These output signal are sent on one side to a V1190A Time to Digital Converter (TDC) module from CAEN and on the other to an OR module to count the number of detected signals. Trigger and hit coïncidences are monitored using scalers. The TDC is used to store the data into ROOT files. These ROOT files are thus analysed to understand the detectors performance.

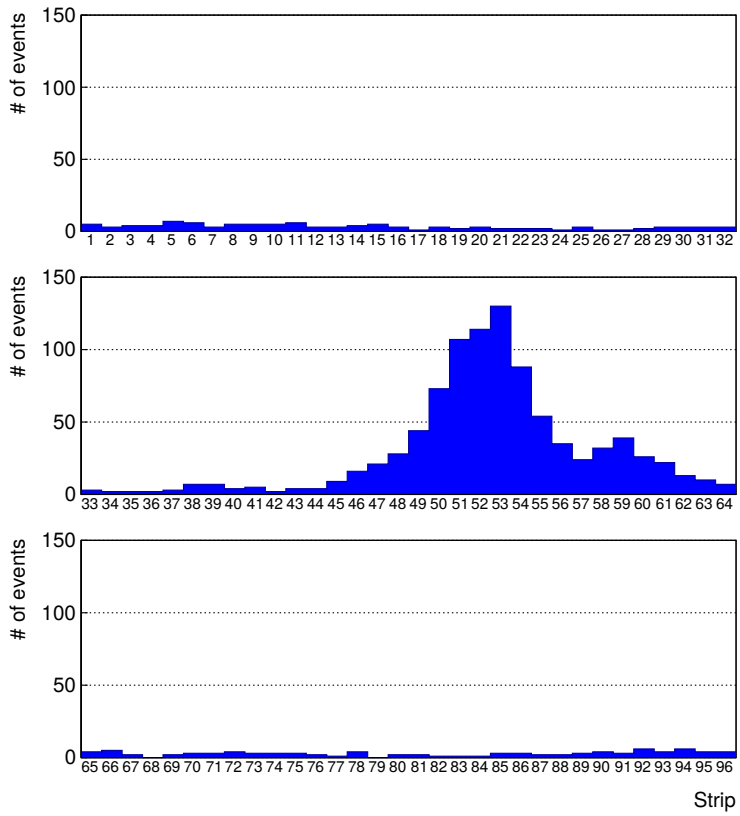

Figure 6.5: Hit distributions over all 3 parttions of RE-4-2-BARC-161 chamber is showed on these plots. Top, middle and bottom figures respectively correspond to partitions A, B, and C. These plots show that some events still occur in other half-partitions than B2, which corresponds to strips 49 to 64, in front of which the trigger is placed, contributing to the inefficiency of detection of cosmic muons. In the case of partitions A and C, the very low amount of data can be interpreted as noise. On the other hand, it is clear that a little portion of muons reach the half-partition B1, corresponding to strips 33 to 48.

6.2.3 Geometrical acceptance of the setup layout to cosmic muons

In order to profit from a constant gamma irradiation, the detectors inside of the GIF bunker need to be placed in a plane orthogonal to the beam line. The muon beam that used to be available was meant to test the performance of detectors under test. This beam not being active anymore, another solution to test detector performance had to be used. Thus, it has been decided to use cosmic muons detected through a telescope composed of two scintillators. Lead blocks were used as shielding to

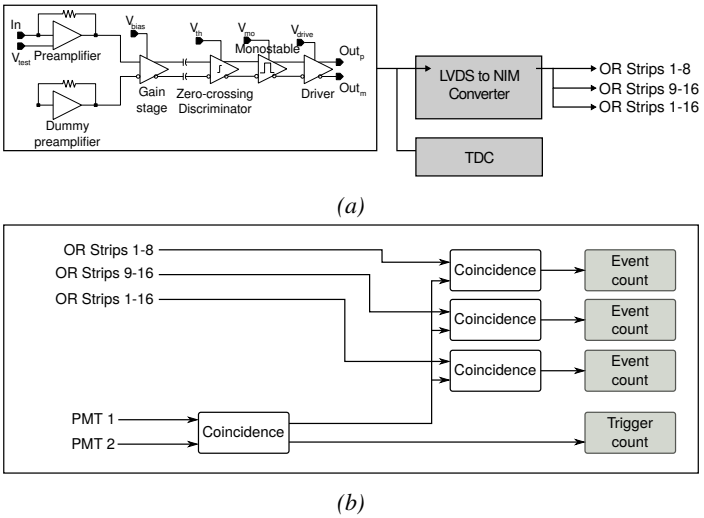

Figure 6.6: Signals from the RPC strips are shaped by the Front End Electronics (FEEs) described on Figure 6.6a. Output LVDS signals are then read-out by a TDC module connected to a computer or converted into NIM and sent to scalers. Figure 6.6b describes how these converted signals are put in coincidence with the trigger.

protect the photomultipliers from gammas as can be seen from Figure 6.4.

An inclination has been given to the cosmic telescope to maximize the muon flux. A good compromise had to be found between good enough muon flux and narrow enough hit distribution to be sure to contain all the events into only one half partitions as required from the limited available readout hardware. Nevertheless, a consequence of the misplaced trigger, that can be seen as a loss of events in half-partition B1 in Figure 6.5, is an inefficiency. Nevertheless, the innefficiency of approximately $20\,\%$ highlighted in Figure 6.8 by comparing the performance of chamber BARC-161 in 904 and at GIF without irradiation seems too important to be explained only by the geometrical acceptance of the setup itself. Simulations have been conducted to show how the setup brings inefficiency.

6.2.3.1 Description of the simulation layout

The layout of GIF setup has been reproduced and incorporated into a Monte Carlo simulation to study the influence of the disposition of the telescope on the final distribution measured by the RPC. A 3D view of the simulated layout is given into Figure 6.9. Muons are generated randomly in a horizontal plane located at a height corresponding to the lowest point of the PMTs. This way, the needed size of the plane in order to simulate events happening at very big azimutal angles (i.e. $\theta \approx \pi$) can be kept relatively small. The muon flux is designed to follow the usual $cos^2\theta$

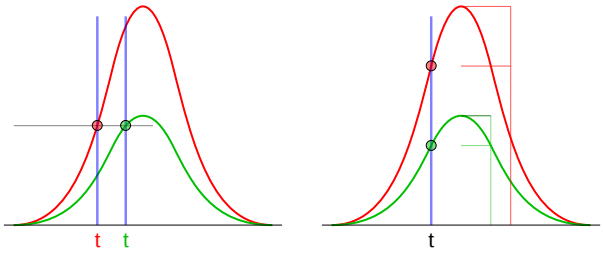

(a)

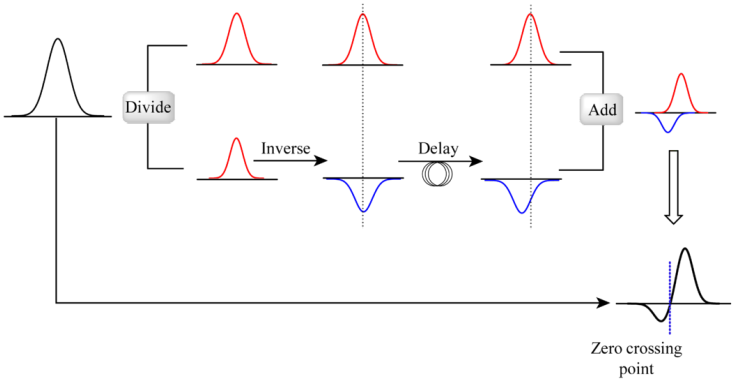

(b)

Figure 6.7: Description of the principle of a CFD. A comparison of threshold triggering (left) and constant franction triggering (right) is shown in Figure 6.7a. Constant franction triggering is obtained thanks to zero-crossing technique as explained in Figure 6.7b. The signal arriving at the input of the CFD is split into three components. A first one is delayed and connected to the inverting input of a first comparator. A second component is connected to the noninverting input of this first comparator. A third component is connected to the noninverting input of another comparator along with a threshold value connected to the inverting input. Finally, the output of both comparators is fed through an AND gate.

distribution for cosmic particle. The goal of the simulation is to look at muons that pass through the muon telescope composed of the two scintilators and define their distribution onto the RPC plane. During the reconstruction, the RPC plane is then divided into its strips and each muon track is assigned to a strip.

In order to further refine the quality of the simulation and understand deeper the results the dependance of the distribution has been studied for a range of telescope inclinations. Moreover, the threshold applied on the PMT signals has been

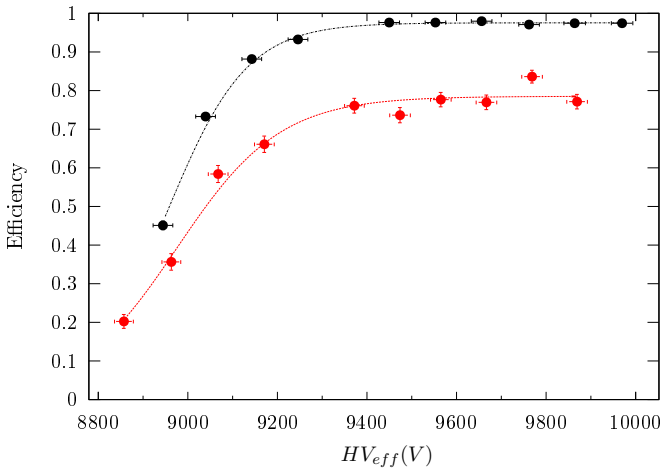

Figure 6.8: Results are derived from data taken on half-partition B2 only. On the 18^{th} of June 2014, data has been taken on chamber RE-2-BARC-161 at building 904 (Prevessin Site) with cosmic muons providing us a reference efficiency plateau of $(97.54 \pm 0.15)\%$ *represented by a black curve. A similar measurement has been done at GIF on the 21^{st} of July with the same chamber giving a plateau of* $(78.52 \pm 0.94)\%$ *represented by a red curve.*

included into the simulation in the form of a cut. In the approximation of uniform scintillators, it has been considered that the threshold can be understood as the minimum distance particles need to travel through the scintillating material to give a strong enough signal. Particles that travel a distance smaller than the set "threshold" are thus not detected by the telescope and cannot trigger the data taking. Finally, the front-end electronics threshold also has been considered in a similar way. The mean momentum of horizontal cosmic rays is higher than those of vertical ones but the stopping power of matter for momenta ranging from $1\,\mathrm{GeV}$ to $1\,\mathrm{TeV}$ stays comparable. It is then possible to assume that the mean number of primary e^-/ion pairs per unit length will stay similar and thus, depending on the applied discriminator threshold, muons with the shortest path through the gas volume will deposit less charge and induce a smaller signal on the pick-up strips that could eventually not be detected. These two thresholds also restrain the overall geometrical acceptance of the system.

6.2.3.2 Simulation procedure

The simulation software has been designed using C++ and the output data is saved into ROOT histograms. Simulations start for a threshold T_{scint} varying in a range

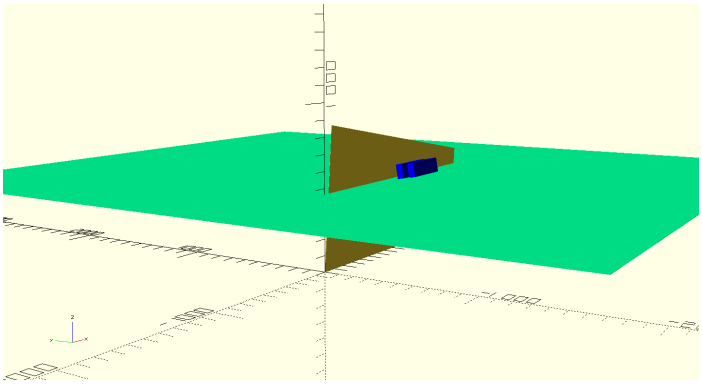

(a)

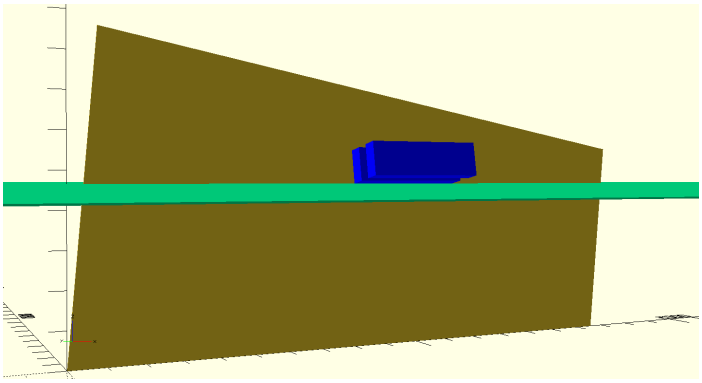

(b)

Figure 6.9: Representation of the layout used for the simulations of the test setup. The RPC is represented as a yellow trapezoid while the two scintillators as blue cuboids looking at the sky. A green plane corresponds to the muon generation plane within the simulation. Figure 6.3a shows a global view of the simulated setup. Figure 6.3b shows a zommed view that allows to see the 2 scintillators as well as the full RPC plane.

from 0 to $45\,\mathrm{mm}$ in steps of $5\,\mathrm{mm}$, where $T_{scint} = 0\,\mathrm{mm}$ corresponds to the case where there isn't any threshold apply on the input signal while $T_{scint} = 45\,\mathrm{mm}$, which is the scintillator thickness, is the case where muons cannot arrive orthogonally onto the scintillator surface. For a given T_{scint}, a set of RPC thresholds are considered. The RPC threshold, T_{RPC} varies from $2\,\mathrm{mm}$, the thickness of the gas volume, to $3\,\mathrm{mm}$ in steps of $0.25\,\mathrm{mm}$. For each (T_{scint};T_{RPC}) pair, $N_\mu = 10^8$ muons are randomly generated inside the muon plane described in the previous paragraph with an azimutal angle θ chosen to follow a $cos^2\theta$ distribution.

Planes are associated to each surface of the scintillators. Knowing muon position into the muon plane and its direction allows us, by assuming that muons travel

in a straight line, to compute the intersection of the muon track with these planes. Applying conditions to the limits of the surfaces of the scintillator faces then gives us an answer to weither or not the muon passed through the scintillators. In the case the muon has indeed passed through the telescope, the path through each scintillator is computed and muons whose path was shorter than T_{scint} are rejected and are thus considered as having not interacted with the setup.

On the contrary, if the muon is labeled as good, its position within the RPC plane is computed and the corresponding strip, determined by geometrical tests in the case the distance through the gas volume was enough not to be rejected because of T_{RPC}, gets a hit and several histograms are filled in order to keep track of the generation point on the muon plane, the intersection points of the reconstructed muons within the telescope, or on the RPC plane, the path traveled through each individual scintillator or the gas volume, as well as other histograms. Moreover, muons fill different histograms weither they are forward or backward coming muons. They are discriminated according to their direction components. When a muon is generated, an (x, y, z) position is assigned into the muon plane as well as a (θ;ϕ) pair that gives us the direction it's coming from. This way, muons satisfying the condition $0 \leq \phi < \pi$ are designated as backward coming muons while muons satisfying $\pi \leq \phi < 2\pi$ as forward coming muons.

This simulation is then repeated for different telescope inclinations ranging in between 4 and 20° and varying in steps of 2°. Due to this inclination and to the vertical position of the detector under test, the muon distribution reconstructed in the detector plane is asymmetrical. The choice as been made to chose a skew distribution formula to fit the data built as the multiplication of gaussian and sigmoidal curves together. A typical gaussian formula is given as 6.1 and has three free parameters as A_g, its amplitude, $\bar{x}$, its mean value and σ, its root mean square. Sigmoidal curves as given by formula 6.2 are functions converging to 0 and A_s as x diverges. The inflexion point is given as x_i and λ is proportional to the slope at $x = x_i$. In the limit where $\lambda \longrightarrow \infty$, the sigmoid becomes a step function.

$$g(x) = A_g e^{\frac{-(x-\bar{x})^2}{2\sigma^2}} \tag{6.1}$$

$$s(x) = \frac{A_s}{1 + e^{-\lambda(x-x_i)}} \tag{6.2}$$

Finally, a possible representation of a skew distribution is given by formula 6.3 and is the product of 6.1 and 6.2. Naturally, here $A_{sk} = A_g \times A_s$ and represents the theoretical maximum in the limit where the skew tends to a gaussian function.

$$sk(x) = g(x) \times s(x) = A_{sk} \frac{e^{\frac{-(x-\bar{x})^2}{2\sigma^2}}}{1 + e^{-\lambda(x-x_i)}} \tag{6.3}$$

6.2.3.3 Results

Influence of $\mathbf{T_{scint}}$ on the muon distribution

Influence of $\mathbf{T_{RPC}}$ on the muon distribution

Influence of the telescope inclination on the muon distribution

Comparison to data taken at GIF without irradiation

6.2.4 Photon flux at GIF

6.2.4.1 Expectations from simulations

In order to understand and evaluate the γ flux in the GIF area, simulations had been conducted in 1999 and published by S. Agosteo et al [4]. Table 6.1 presented in this article gives us the γ flux for different distances D to the source. This simulation was done using GEANT and MCNP, a Monte Carlo N-particle transport code, and the flux F is given in number of γ per unit area and unit time along with the estimated error from these packages expressed in %.

Nominal ABS	Photon flux F [$\mathrm{s^{-1}cm^{-2}}$]			
	at D = 50 cm	at D = 155 cm	at D = 300 cm	at D = 400 cm
1	$0.12 \cdot 10^8 \pm 0.2\%$	$0.14 \cdot 10^7 \pm 0.5\%$	$0.45 \cdot 10^6 \pm 0.5\%$	$0.28 \cdot 10^6 \pm 0.5\%$
2	$0.68 \cdot 10^7 \pm 0.3\%$	$0.80 \cdot 10^6 \pm 0.8\%$	$0.25 \cdot 10^6 \pm 0.8\%$	$0.16 \cdot 10^6 \pm 0.6\%$
5	$0.31 \cdot 10^7 \pm 0.4\%$	$0.36 \cdot 10^6 \pm 1.2\%$	$0.11 \cdot 10^6 \pm 1.2\%$	$0.70 \cdot 10^5 \pm 0.9\%$

Table 6.1: Total photon flux ($E\gamma \leq 662\,\mathrm{keV}$) with statistical error predicted considering a ^{137}Cs activity of 740 GBq at different values of the distance D to the source along the x-axis of irradiation field [4].

The simulation doesn't directly provides us with an estimated flux at the level of our RPC. First of all, it is needed to extract the value of the flux from the available data contained in the original paper and then to estimate the flux in 2014 at the time the experimentation took place. Figure 6.10 that contains the data from Table 6.1. In the case of a pointlike source emiting isotrope and homogeneous gamma radiations, the gamma flux F at a distance D to the source with respect to a reference point situated at D_0 where a known flux F_0 is measured will be

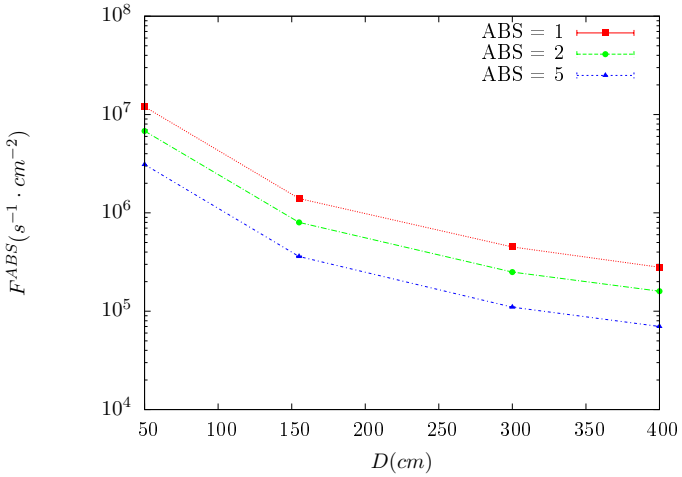

Figure 6.10: γ flux $F(D)$ is plot using values from table 6.1. As expected, the plot shows similar attenuation behaviours with increasing distance for each absorption factors.

expressed like in Equation 6.4, assuming that the flux decreases as $1/D^2$, where c is a fitting factor.

$$F^{ABS} = F_0^{ABS} \times \left(\frac{cD_0}{D}\right)^2 \tag{6.4}$$

By rewriting Equation 6.4, it comes that :

$$c = \frac{D}{D_0}\sqrt{\frac{F^{ABS}}{F_0^{ABS}}} \tag{6.5}$$

$$\Delta c = \frac{c}{2}\left(\frac{\Delta F^{ABS}}{F^{ABS}} + \frac{\Delta F_0^{ABS}}{F_0^{ABS}}\right) \tag{6.6}$$

Finally, using Equation 6.5 and the data in Table 6.1 with $D_0 = 50\,\mathrm{cm}$ as reference point, we can build Table 6.2. It is interesting to note that c for each value of D doesn't depend on the absorption factor.

For the range of D/D_0 values available, it is possible to use a simple linear fit to get the evolution of c. The linear fit will then use only 2 free parameters, a and b, as written in Equation 6.7. This gives us the results showed in Figure 6.11. Figure 6.11b confirms that using only a linear fit to extract c is enough as the evolution of the rate that can be obtained superimposes well on the simulation points.

Nominal ABS	Correction factor c		
	at D = 155 cm	at D = 300 cm	at D = 400 cm
1	$1.059 \pm 0.70\%$	$1.162 \pm 0.70\%$	$1.222 \pm 0.70\%$
2	$1.063 \pm 1.10\%$	$1.150 \pm 1.10\%$	$1.227 \pm 0.90\%$
5	$1.056 \pm 1.60\%$	$1.130 \pm 1.60\%$	$1.202 \pm 1.30\%$

Table 6.2: Correction factor c is computed thanks to formulae 6.5 taking as reference $D_0 = 50\,\mathrm{cm}$ and the associated flux F_0^{ABS} for each absorption factor available in table 6.1.

$$c\left(\frac{D}{D_0}\right) = a\frac{D}{D_0} + b \tag{6.7}$$

$$F^{ABS} = F_0^{ABS}\left(a + \frac{bD_0}{D}\right)^2 \tag{6.8}$$

$$\Delta F^{ABS} = F^{ABS}\left[\frac{\Delta F_0^{ABS}}{F_0^{ABS}} + 2\frac{\Delta a + \Delta b\frac{D_0}{D}}{a + \frac{bD_0}{D}}\right] \tag{6.9}$$

In the case of the 2014 GIF tests, the RPC plane is located at a distance D =206 cm to the source. Moreover, to estimate the strength of the flux in 2014, it is necessary to consider the nuclear decay through time assiciated to the Cesium source whose half-life is well known ($t_{1/2} = (30.05 \pm 0.08)\,\mathrm{y}$). The very first source activity measurement has been done on the 5^{th} of March 1997 while the GIF tests where done in between the 20^{th} and the 31^{st} of August 2014, i.e. at a time $t = (17.47 \pm 0.02)\,\mathrm{y}$ resulting in an attenuation of the activity from 740 GBq in 1997 to 494 GBq in 2014. All the needed information to extrapolate the flux through our detector in 2014 has now been assembled, leading to the Table 6.3. It isinteresting to note that for a common RPC sensitivity to γ of $2 \cdot 10^{-3}$, the order of magnitude of the estimated hit rate per unit area is of the order of the kHz for the fully opened source. Moreover, taking profit of the two working absorbers, it will be possible to scan background rates at 0 Hz, ∼300 Hz as well as ∼600 Hz. Without source, a good estimate of the intrinsic performance will be available. Then at 300 Hz, the goal will be to show that the detectors fulfill the performance certification of CMS RPCs. Then a first idea of the performance of the detectors at higher background will be provided with absorbtion factors 2 (∼600 Hz) and 1 (no absorbtion). ***[Here I will also put a reference to the plot showing the estimated background rate at the level of RE3-1 in the case of HL-LHC but this one being in another chapter, I will do it later.]***

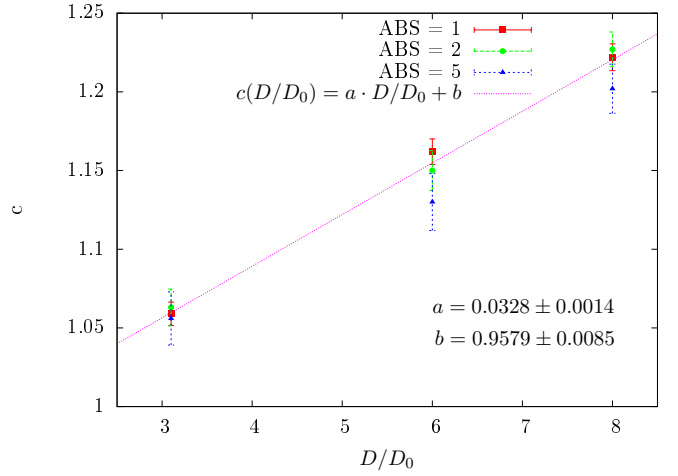

(a)

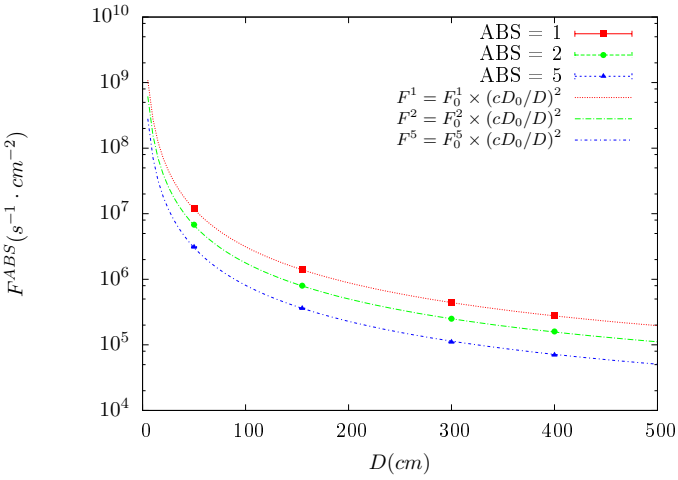

(b)

Figure 6.11: Figure 6.11a shows the linear approximation fit done via formulae 6.7 on data from table 6.2. Figure 6.11b shows a comparison of this model with the simulated flux using a and b given in figure 6.11a in formulae 6.4 and the reference value $D_0 = 50cm$ and the associated flux for each absorption factor F_0^{ABS} from table 6.1

6.2.4.2 Dose measurements

6.3 Consolidation tests at GIF++

6.4 Results and discussions

6.4.1 Preliminary studies results

6.4.2 Consolidation studies results

Nominal ABS	Photon flux F [$\mathrm{s^{-1}cm^{-2}}$] at D_0^{1997} = 50 cm	at D^{1997} = 206 cm	at D^{2014} = 206 cm	Hit rate/unit area [$\mathrm{Hz\,cm^{-2}}$] at D^{2014} = 206 cm
1	$0.12 \cdot 10^8 \pm 0.2\%$	$0.84 \cdot 10^6 \pm 0.3\%$	$0.56 \cdot 10^6 \pm 0.3\%$	1129 ± 32
2	$0.68 \cdot 10^7 \pm 0.3\%$	$0.48 \cdot 10^6 \pm 0.3\%$	$0.32 \cdot 10^6 \pm 0.3\%$	640 ± 19
5	$0.31 \cdot 10^7 \pm 0.4\%$	$0.22 \cdot 10^6 \pm 0.3\%$	$0.15 \cdot 10^6 \pm 0.3\%$	292 ± 9

Table 6.3: The data at D_0 in 1997 is taken from [4]. In a second step, using Equations 6.8 and 6.9, the flux at D can be estimated in 1997. Then, taking into account the attenuation of the source activity, the flux at D can be estimated at the time of the tests in GIF in 2014. Finally, assuming a sensitivity of the RPC to γ $s = 2 \cdot 10^{-3}$, an estimation of the hit rate per unit area is obtained.

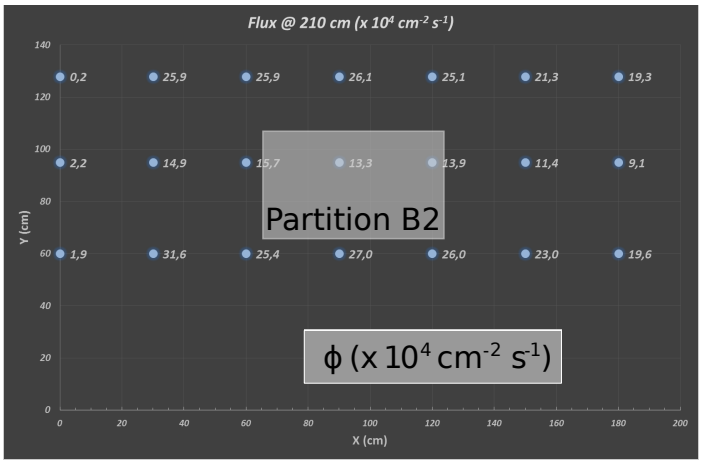

Figure 6.12: Dose measurements has been done in a plane corresponding to the tents front side. This plan is 1900 mm away from the source. As explained in the first chapter, a lens-shaped lead filter provides a uniform photon flux in the vertical plan orthogonal to the beam direction. If the second line of measured fluxes is not taken into account because of lower values due to experimental equipments in the way between the source and the tent, the uniformity of the flux is well showed by the results.

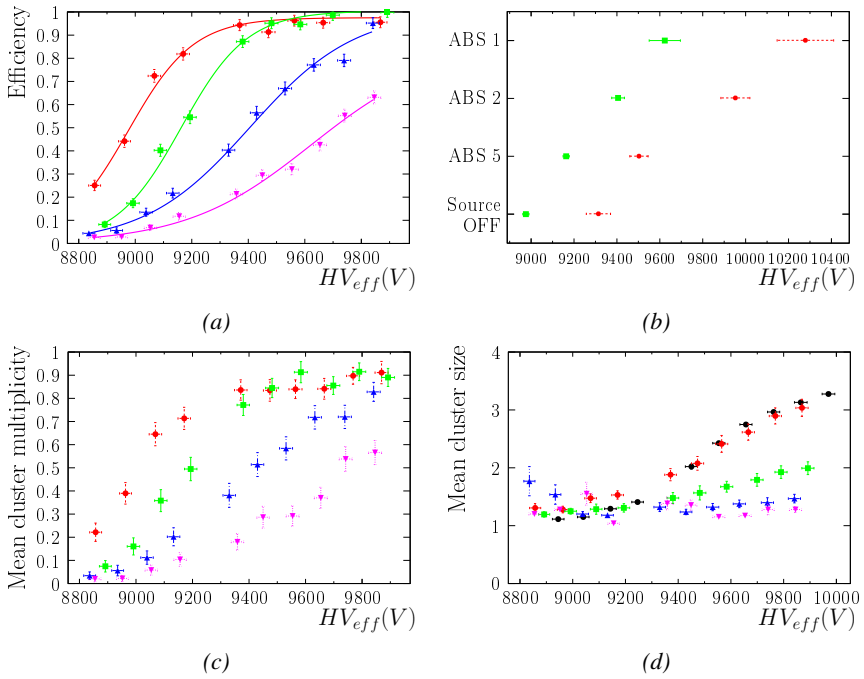
Efficiency
$HV_{eff}(V)$
(a)
ABS 1
ABS 2
ABS 5
Source OFF
$HV_{eff}(V)$
(b)
Mean cluster multiplicity
$HV_{eff}(V)$
(c)
Mean cluster size
$HV_{eff}(V)$
(d)

Figure 6.13

7 Simulating a RPC

7.1 Garfield++ simulation

7.2 Hybrid simulation

7.3 Results and discussions

8

Conclusions and outlooks

8.1 Conclusions

8.2 Outlooks

References

[1] CERN. Geneva. LHC Experiments Committee. *The CMS muon project : Technical Design Report*. Tech. rep. CERN-LHCC-97-032. CMS Collaboration, 1997.

[2] CERN. Geneva. LHC Experiments Committee. *Technical Proposal for the Phase-II Upgrade of the CMS Detector*. Tech. rep. CERN-LHCC-2015-010. CMS Collaboration, 2015.

[3] CERN. Geneva. LHC Experiments Committee. *CMS, the Compact Muon Solenoid : technical proposal*. Tech. rep. CERN-LHCC-94-38. CMS Collaboration, 1994.

[4] S. Agosteo et al. "A facility for the test of large-area muon chambers at high rates". In: *NIMA* 452 (2000), pp. 94–104.

A

A data acquisition software for VME CAEN TDCs

A.1 Introduction

Start text here...

B

Details on the online analysis package

B.1 Introduction

insert text here

C

Structure of the hybrid simulation software

C.1 Introduction

insert text here...